

Joint fan-beam CT and Compton scattering tomography: analysis and image reconstruction

Kuger, L.¹ and Rigaud, G.²

¹Institut für Mathematik, Julius-Maximilians-Universität Würzburg

²Zentrum für Technomathematik, Universität Bremen, Germany

July 2020

ABSTRACT

The recent development of energy-resolving cameras opens the way to new types of applications and imaging systems. In this work, we consider computerized tomography (CT) with fan-beam geometry and equipped with such cameras. The measured radiation is then a function of the positions of the source and detectors and of the energy of the incoming photons. Due to the Compton effect, the variations in energy (or spectrum) of the measurement are modeled in terms of scattering events leading to the so-called Compton scattering tomography (CST). We propose an analysis of the spectral data in terms of modelling and mapping properties which results in a general reconstruction strategy. Thanks to the supplementary information given by the energy, this joint CT-CST scanner makes accurate reconstructions of characteristics of the sought-for object possible for very few source positions and a small number of detectors. The general reconstruction strategy is finally validated on synthetic data via a total variation iterative scheme. Also illustrative, this work motivates the potential of combining conventional CT and Compton scattering imaging (CSI) with various architectures in 2D and 3D.

1 Introduction

In conventional CT, an X-ray source emits ionizing radiation towards an object under study while detectors located outside the object measure variations in the intensity of the incoming photon flux. These variations are due to the resistance of the medium to the propagation of the photon beam and deliver precious information used to image the inner part of the scanned specimen. More precisely, considering photons of the same energy E , the intensity of the corresponding photon beam at a point \mathbf{x} propagating in direction θ , noted here $I(\mathbf{x}, \theta)$, satisfies the following stationary transport equation

$$\theta^T \nabla_x I(\mathbf{x}, \theta) + \mu_E(\mathbf{x}) I(\mathbf{x}, \theta) = 0, \quad \mathbf{x} \in \Omega \subset \mathbb{R}^2 \quad (1)$$

in which $\mu_E(\mathbf{x})$ stands for the linear attenuation coefficient. This latter can be understood as the sum of the physical processes occurring between photons and matter inside the medium under study. These different processes include incoherent and coherent scattering events (e.g. Compton, Rayleigh or Thomson scattering), photoelectric absorption and pair production, see section 2.3 in [15], and can be quantified by the energy and the atomic number Z , i.e. the nature of the material. For typical applications of CT, the initial photon energies vary between 80-140keV (clinical CT) up to 9 MeV (industrial testing for large objects) [27]. Restricting to this interval of energies it can be argued that, depending of course still on the scanned materials, the predominant of the physical interaction processes are only the photoelectric absorption and the Compton effect cf. [15, 25]. Following on from Stonestrom et al [25], one can model the linear attenuation coefficient as

$$\mu_E(\mathbf{x}) = \mu^{\text{PE}}(\mathbf{x}; E) + \sigma^{\text{C}}(E) n_e(\mathbf{x}) \quad (2)$$

where $\mu^{\text{PE}}(\mathbf{x}; E)$ is the contribution of the photoelectric effect and $\mu^{\text{C}}(\mathbf{x}; E) = \sigma^{\text{C}}(E)n_e(\mathbf{x})$ of the Compton effect. Hereby, $\sigma^{\text{C}}(E)$ is the total cross section of the Compton effect at energy E and $n_e(\mathbf{x})$ the electron density of the material at the point \mathbf{x} .

Out of these two phenomena, the Compton effect is the dominant one when the energy of the source is sufficiently large. For materials typical in human bodies, energies larger than 200keV are sufficient, however for larger- Z materials the energy has to be even larger [15]. In this work, we will assume therefore initial energies around 1MeV such that μ^{PE} can be neglected and we will thus model the attenuation coefficient by

$$\mu_E(\mathbf{x}) = \sigma^{\text{C}}(E)n_e(\mathbf{x}). \quad (3)$$

This approximation will simplify our analysis as the notions of linear attenuation and electron density can then be exchanged equivalently for a monochromatic source $\sigma^{\text{C}}(E)$ being independent of \mathbf{x} .

While the photoelectric effect describes the absorption of photons by the atomic structure, the Compton effect stands for the inelastic (in the sense that there is a transfer of energy in the process) collision of photons and electrons. Depicted in figure 1.1, a scattered photon hits an electron, its trajectory changes by an angle ω and it transfers part of its energy to the recoiled electron. In particular, in contrast to radiation absorbed by the photoelectric effect, a large part of the scattered photons reaches the detector surface and can be measured there. The nature of Compton scattering tomography (CST) is then to exploit these scattered photons when standard CT focuses on the primary (or ballistic) radiation, i.e. photons which crossed the object without interactions.

The Compton formula states the relation between the scattering angle and the energy loss of the photon by

$$E_\omega = \frac{E_0}{1 + \frac{E_0}{m_e c^2}(1 - \cos \omega)}, \quad (4)$$

where $m_e c^2$ is an electron's energy at rest and E_0 is the photon energy prior to the scattering. The scattering can occur for all $\omega \in (0, \pi]$, the probability for a photon scattered in a certain angle being given by the differential cross section $\frac{d\sigma}{d\Omega}(\omega)$ first deduced by Klein and Nishina 1929 in [11]. Furthermore, photons are of course not restricted to a single scattering event, and some measured photons are scattered twice or more times. This shows that the energy spectrum measured at a detector will in fact be polychromatic, where the highest possible energy E_0 comes from the primary radiation and the scattered photons create a broad spectrum of energies lower than this value. Examining the structure of the spectrum is crucial in understanding the way photons are scattered during the acquisition process and therefore in designing a suited reconstruction technique.

Following these explanations, a photon measured with an energy smaller than the initial energy E_0 was in our model scattered and changed its direction somewhere in the object. It therefore does not contain information about the attenuation map on only a straight line from the source \mathbf{s} to the detector \mathbf{d} . The energy 'encodes' information on the way the photon passed through the object, we therefore want to measure it for each incoming photon and build a mathematical model of the relation between energy and trajectory of the photon.

Until recently, the cameras used in CT were only able to measure the intensity of the incoming photon flux ignoring others parameters such as the energy. Since the 1960s, the technology in semiconductor detectors experienced rapid developments due to the need of good radiation detectors in spectroscopy and particle detectors [12]. The high resolution of e.g. silicon or germanium crystal detectors in both space and energy dimensions meanwhile also opens doors to new imaging techniques. Their ability of distinguishing photons of different levels of energies is a fundamental requirement of Compton scattering tomography and throughout this paper we assume that radiation detectors with a certain energy resolution are available in the data acquisition process.

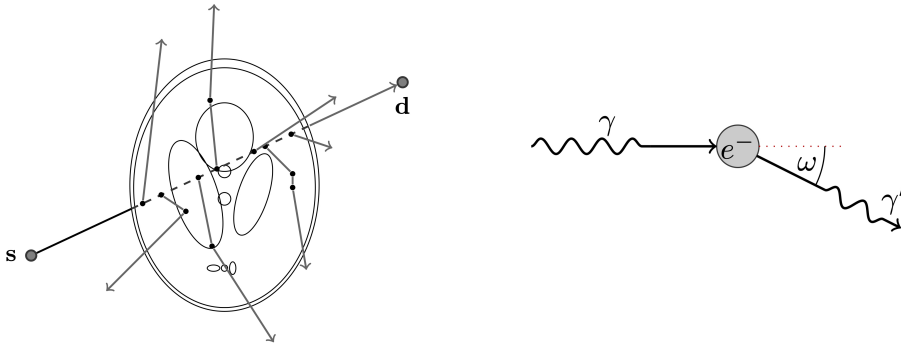


Figure 1.1: Scattering effects reduce the intensity of the ballistic radiation. On the right, the Compton effect is illustrated. The number of scattered photons depends on the density of electrons in the material and the cross section σ^C , as in (2) and (3)

The first step in a mathematical model of the spectrum Spec is the distinction by number of scattering events. Denoting by g_0 the primary part of the measured radiation, the detected photon flux at a non-collimated camera can be represented as

$$\text{Spec}(\mathbf{s}, \mathbf{d}, E) = \sum_{i=0}^{\infty} g_i(\mathbf{s}, \mathbf{d}, E) \quad (5)$$

where g_i stands for the photons scattered exactly i times.

In the research of Compton scattering tomography, there has been a lot of recent work on the modeling, the properties and the use of g_1 for reconstruction purposes [18, 28, 19, 20, 5]. But, as a mathematical modeling of the higher-order terms g_2, g_3, \dots seems to be rather complicated, up to the authors' knowledge there is at this point few theory on how to recover the object from the whole spectrum Spec .

Focusing on the 2D case, this manuscript strives to extend the study from [21] by introducing operators that model the g_i for $i = 0, 1, 2$. Due to the complexity of the model, we restrict to these first terms and approximate

$$\text{Spec} \approx g_0 + g_1 + g_2 + \eta =: \mathfrak{S}(n_e), \quad (6)$$

where η models the higher-order terms and potential noise at the same time. We aim to tackle the noise by applying regularization techniques in the reconstruction process. This leads to the task of solving optimization problems of the form

$$\min_{n_e} R_\gamma(n_e) \quad \text{s.t.} \quad \mathcal{D}(\text{Spec}) = \mathcal{D}(\mathfrak{S}(n_e)), \quad (7)$$

where R_γ is some penalizing function, for instance some (approximated) norm or semi-norm in a suited Banach space, and \mathcal{D} is an operator that pre-processes the spectrum, e.g. solely the identity operator or, as we propose, a suited differential operator.

The reconstruction strategy developed in this manuscript extends naturally to the rest of the spectrum. The nature of the spectrum leads to combine CT (obtained through the component g_0) and CST (which is based on g_1) in order to solve our general inverse problem described above. In the proposed architecture, one considers a fan-beam geometry CT-scan with sparse source and detectors positions. The system is then enhanced by assuming the detectors to be energy-resolved. While the sparse inverse problem corresponding to g_0 can be solved by compressed sensing techniques at the cost of a poor accuracy, it delivers a precious approximation of the electron density n_e . The latter will then be used in our study of g_1 and g_2 and finally to solve the studied inverse problem via iterative schemes regularized by variational methods.

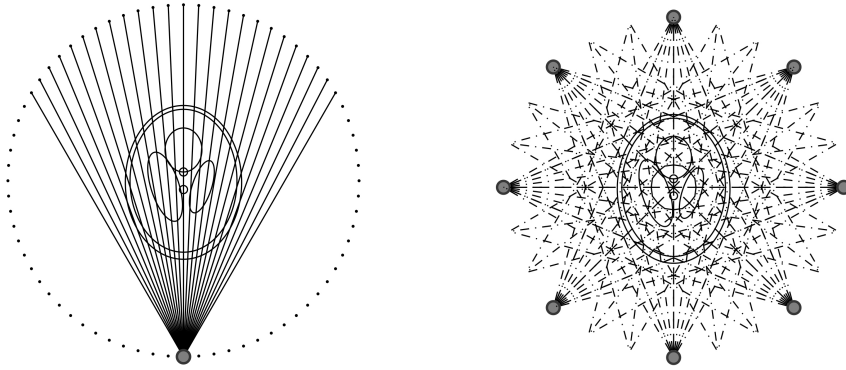


Figure 2.1: The scanning geometry used throughout the article. On the left, a single source is projecting to several detectors which are placed on a circle. To prevent limited data problems, we consider several source positions which creates a sampling of the object as sketched in the right picture.

The organisation of the paper is as follows. Section 2 will begin by recalling the principles of CT image reconstruction. In the case of a very limited number of source positions and detectors, techniques from compressed sensing will be used to recover approximate images from CT data in 2.1. As the results are not satisfying due to the limited data, we will proceed by incorporating information on the rest of the spectrum. For this sake, we model the mathematical representation of g_1 and g_2 in 2.2 resp. 2.3. The section ends by reviewing results from [21] on the mapping properties of the operators describing g_1 and g_2 in 2.4. These mapping properties induce the main idea of our algorithm, namely preprocessing the spectrum with a derivative with respect to the energy variable, hoping to cancel out smoother parts as much as possible. The algorithm itself is then derived and corresponding reconstructions of an image phantom are illustrated in the following section 3.

2 Analysis of the Spectral Data

This section will be devoted to model the function \mathfrak{S} given in eq. (6). While the study of this non-linear operator would be too complex on its own, we propose to study its components, namely g_0 , g_1 and g_2 corresponding respectively to the ballistic (primary) radiation, the first-order scattering and the second-order scattering. While g_0 can be understood as standard CT data, we then study the behaviours of g_1 and g_2 using Fourier integral operators and their mapping properties. These results show that focusing on g_1 and its model provides an elegant alternative to solve directly $\mathfrak{S}(n_e) = \text{Spec}$ which is much more complex in terms of computation and analysis. This alternative way will be illustrated in Section 3.

The scanning geometry used throughout our analysis and simulations is depicted in figure 2.1. The object, characterized by its electron density n_e , is supported in a disk Ω . Several gamma cameras are positioned on the surrounding circle, e.g. S^1 . The radiation source, positioned on the same circle, isotropically emits high-energetic photons and is moved to different positions around the object to prevent limited data problems. This leads to fan-beam projection data for the standard-CT case. Characteristic for the scanning geometry is hereby its low number of source positions and corresponding detectors, to be precise, the total number of different source - detector pairs will be around $2N$ for a reconstructed image of N^2 pixels. This small number makes it impossible to reconstruct the object from the CT data alone, which is why we need to incorporate spectral information.

2.1 Ballistic Data

By integrating the transport equation eq. (1) along straight lines, we can describe the intensity loss in terms of the linear attenuation coefficient μ_E and obtain the famous Beer-Lambert law. It states that the directed beam intensity decays exponentially on the way from a point $\mathbf{x} \in \Omega \subset \mathbb{R}^2$ to another point $\mathbf{y} := \mathbf{x} + t\theta \in \Omega$, where $\theta \in \mathbb{R}^2 \setminus \{0\}$:

$$\frac{I(\mathbf{y})}{I(\mathbf{x})} = \exp\left(-\int_0^t \mu_E(\mathbf{x} + s\theta) ds\right) \quad (8)$$

The Beer-Lambert law directly reveals the mathematical inverse problem hidden behind CT. Our goal is to reconstruct the attenuation map μ_E from its line integrals, the so-called X-Ray transform denoted here as \mathcal{P} . The data is given for different source positions \mathbf{s} and several directions θ , each corresponding to a detector $\mathbf{d}(\mathbf{s}, \theta)$ at $\mathbf{s} + T\theta$, i.e.

$$-\log\left(\frac{I(\mathbf{d})}{I(\mathbf{s})}\right) = -\log\left(\frac{g_0(\mathbf{s}, \mathbf{d}(\mathbf{s}, \theta))}{I(\mathbf{s})}\right) = \mathcal{P}\mu_E(\mathbf{s}, \mathbf{d}(\mathbf{s}, \theta)) = \int_0^T \mu_E(\mathbf{s} + t\theta) dt. \quad (9)$$

The arising inverse problem, the task to recover μ_E from g , is then solved by analytic or iterative image reconstruction methods.

In this scenario, we need to find f from g with $\mathcal{P}f = -\log(g_0/I(\mathbf{s}))$ when the size of g_0 is much smaller than the size of f , i.e. when the problem is very underdetermined. Solving such a system by an FBP method would lead to many local artifacts and a bad image quality. Instead, we may try to use techniques from compressed sensing to recover the image at least approximately. Possible ways to do this are e.g. minimizing the L^1 -norm, the BV-norm or the total variation of the image simultaneously to minimizing the data error. We choose to compute the minimizer

$$\mu_{E_0}^\lambda = \sigma^c(E_0)n_e^\lambda = \arg \min_f \frac{1}{2} \|\mathcal{P}f + \log(g_0/I(\mathbf{s}))\|_{L^2}^2 + \lambda \text{TV}(f), \quad (10)$$

where the total variation of f is given by its usual definition

$$\text{TV}(f) := \sup \left\{ \int_{\Omega} f \operatorname{div} h \, dx \mid g \in C_0^1(\Omega, \mathbb{R}^n) : |h(x)| \leq 1 \, \forall x \in \Omega \right\}. \quad (11)$$

As the dimension of the system is rather small due to the few projection angles, we can easily solve the problem using e.g. a simple gradient descent.

Our test image is a sum of characteristic functions of ellipses with different sizes and opacities, taken from [7]. For the grey values, we use electron densities similar to those of typical different materials in a human thorax taken from [10]:

ellipses in figure 2.2	1	2,6	3,4	5	7
n_e/n_e^{water}	1.077	1.784	0.380	0.906	1.115

We compute the X-Ray transform for 16 sources and 32 detectors each (i.e. 512 projections), with the scanning geometry depicted in figure 2.1 and try to recover a 256×256 image from the data. The results are depicted in figure 2.2.

From this point on, we want to improve the reconstruction by incorporating information on the rest of the spectrum. Note that this means that the architecture of the scanner stays the same and no further sources or detectors are added to the geometry. The number of 'projections', i.e. the number of data points available, will of course be a multiple of 512 as soon as we use the energy resolution in the detectors.

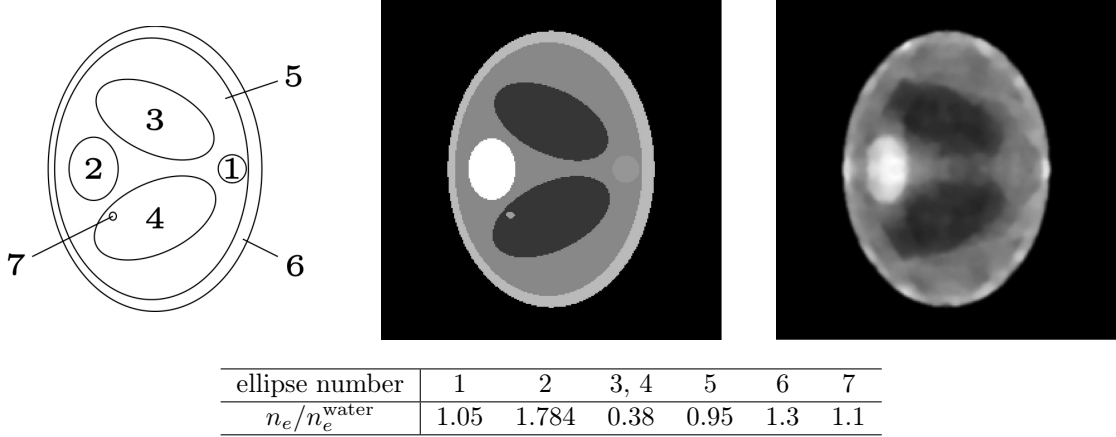


Figure 2.2: In the middle is the ground truth image of the synthetic thorax phantom, with the respective ellipses numbered for reference on the left. The grey values are given as ratio of the resp. electron density over the electron density of water $n_e^{\text{water}} = 3.343 \cdot 10^{23} \text{cm}^{-3}$. On the right, the approximate solution of problem (10) by a gradient descent. It is clear that the limited data is by far not sufficient to recover the object.

2.2 First Order Scattering

Our goal is to define the operator describing the first order scattering, i.e. the photons that are emitted at the source \mathbf{s} with initial energy E_0 , scattered exactly once somewhere along its path and then measured at \mathbf{d} with energy E_ω . From the Compton formula eq. (4), the scattering angle ω can be expressed by.

$$\omega = \cos^{-1} \left(1 - mc^2 \left(\frac{1}{E_\omega} - \frac{1}{E_0} \right) \right) \quad (12)$$

as \cos is bijective on $[0, \pi]$. For a given energy E_ω and fixed \mathbf{s} and \mathbf{d} , the set of points \mathbf{x} for which the angle between $\mathbf{x} - \mathbf{s}$ and $\mathbf{d} - \mathbf{x}$, denoted $\angle(\mathbf{x} - \mathbf{s}, \mathbf{d} - \mathbf{x})$, equals ω , characterizes the locus of scattering events (see figure 2.3) and is denoted by

$$\mathfrak{C}(\omega, \mathbf{d}, \mathbf{s}) = \{\mathbf{x} \in \mathbb{R}^2 : \angle(\mathbf{x} - \mathbf{s}, \mathbf{d} - \mathbf{x}) = \omega\}. \quad (13)$$

Having elaborated a representation of all possible scattering points yielding the same measured energy, we must still model how many of the photons scattered at a specific point \mathbf{x} will be measured by the detector \mathbf{d} .

For this sake, we follow the modeling in [4, 21]: Let I_0 be the initial beam intensity, i.e. the number of photons emitted at \mathbf{s} in the direction of a space element $d\mathbf{x}$. Then the flux's density at \mathbf{x} is reduced due to photometric dispersion and the linear attenuation on the path between \mathbf{s} and \mathbf{x} . We can model this by multiplying the initial intensity by the factor

$$A_E(\mathbf{s}, \mathbf{x}) := \|\mathbf{s} - \mathbf{x}\|^{-2} \exp \left(- \|\mathbf{s} - \mathbf{x}\| \int_0^1 \mu_E(\mathbf{s} + t(\mathbf{x} - \mathbf{s})) dt \right). \quad (14)$$

The ratio of photons scattered at the volume $d\mathbf{x}$ with an angle ω in the direction of \mathbf{d} is given by the Klein-Nishina differential cross section [11] $\frac{d\sigma^C}{d\Omega}(\omega) = r_e^2 P(\omega)$ where $P(\omega)$ is sometimes called Klein-Nishina probability and $d\Omega$ is a solid angle element. Then again, the beam intensity is reduced due to photometric dispersion and linear attenuation between \mathbf{x} and \mathbf{d} . Altogether, the number of detected photons N at \mathbf{d} satisfies

$$dN(\mathbf{s}, \mathbf{d}, \mathbf{x}) = I_0 r_e^2 A_{E_0}(\mathbf{s}, \mathbf{x}) A_{E_\omega}(\mathbf{x}, \mathbf{d}) P(\omega) n_e(\mathbf{x}) d\mathbf{x}. \quad (15)$$

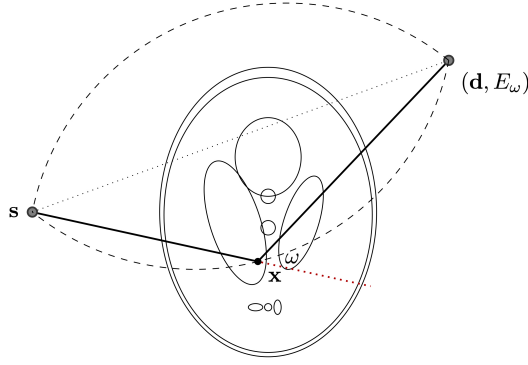


Figure 2.3: Geometry of the first order scattering

We can now put our results together for a representation of the first order scattered data. By integrating the relation eq. (15) over all possible scattering sites \mathbf{x} that yield the same measured energy E_ω at \mathbf{d} , we obtain that

$$g_1(E_\omega, \mathbf{s}, \mathbf{d}) \sim \mathcal{T}_1(n_e)(\omega, \mathbf{s}, \mathbf{d}) := \int_{\mathfrak{C}(\omega, \mathbf{s}, \mathbf{d})} w_1(n_e)(\mathbf{x}, \mathbf{d}, \mathbf{s}) n_e(\mathbf{x}) d\mathbf{x}$$

where the weight function $w_1(n_e)(\mathbf{x}, \mathbf{d}, \mathbf{s}) = P(\omega)A_{E_0}(\mathbf{s}, \mathbf{x})A_{E_\omega}(\mathbf{x}, \mathbf{d})$ gathers the dispersion and attenuation factors in the model. Note that, by its definition in eq. (14), A_E and therefore w_1 depend on the linear attenuation coefficient or, in our model equivalently, on the electron density. The operator \mathcal{T}_1 is therefore nonlinear.

To obtain a more convenient representation of the operator in order to later be able to analyze its mapping properties, we introduce a suited change of variable similarly as proven in [23]. The circular arcs are therein parametrized by

$$\mathbf{x} \in \mathfrak{C}(\omega, \mathbf{s}, \mathbf{d}) \Leftrightarrow \cot \omega = \phi(\mathbf{x} - \mathbf{s}, \mathbf{d} - \mathbf{s})$$

where the characteristic function ϕ is given by

$$\phi(a, b) := \frac{\kappa(a, b) - \rho(a, b)}{\sqrt{1 - \kappa(a, b)^2}}, \quad (16)$$

$$\kappa(a, b) := \frac{a^T b}{\|a\| \|b\|}, \quad \rho(a, b) := \frac{\|a\|}{\|b\|}. \quad (17)$$

By the properties of the Dirac delta distribution δ , we can reformulate

$$\mathcal{T}_1(n_e)(\omega, \mathbf{s}, \mathbf{d}) = \int_{\Omega} \mathcal{W}_1(n_e)(\mathbf{x}, \mathbf{d}, \mathbf{s}) n_e(\mathbf{x}) \delta(\cot \omega - \phi(\mathbf{x} - \mathbf{s}, \mathbf{d} - \mathbf{s})) d\mathbf{x}. \quad (18)$$

where the weight function depending on the electron density is now given by

$$\mathcal{W}_1(n_e)(\mathbf{x}, \mathbf{d}, \mathbf{s}) := \|\nabla_{\mathbf{x}} \phi(\mathbf{x}, \mathbf{d}, \mathbf{s})\| w_1(n_e)(\mathbf{x}, \mathbf{d}, \mathbf{s}).$$

After establishing the representation of g_1 , we now have to do the same for the number of photons scattered exactly twice g_2 .

2.3 Second Order Scattering

The construction of the operator modeling g_2 will follow a comparable strategy as in the case of the first order scattering.

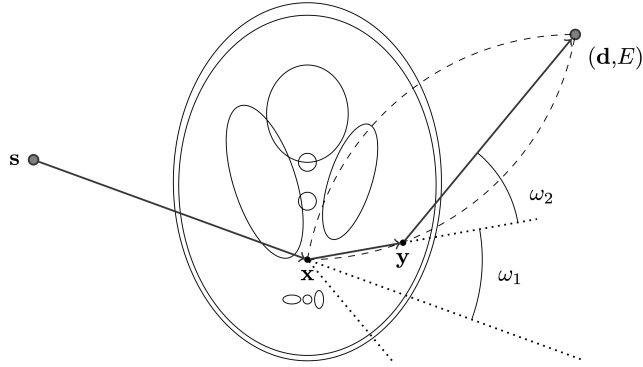


Figure 2.4: Geometry of the second order scattering

First, the possible scattering points for a fixed, measured energy E have to be identified, which is in this case more complicated as the second scattering site depends of course on the first one. The main idea of this construction is to temporarily fix the first scattering site and scattering angle. The Compton formula then yields the second scattering angle and we can explicitly compute the second point in Lemma 1 by some geometrical considerations illustrated also in figure 2.4. After that we extend equation (15) into a formulation for the variation of measured photons that are scattered twice in the object. Integrating the equation over the set of possible scattering sites finally establishes the operator describing g_2 , which will be done in Theorem 2. Eventually, we derive a similar representation as for \mathcal{T}_1 in eq. (18) defining a characteristic function that relates a fixed energy E to an integration set in $\Omega \times \Omega$.

To begin with, we compute the relation between the scattering angles given a measured photon energy E . Assume that the photon is emitted at the point source \mathbf{s} with initial energy E_0 and first scattered at the point \mathbf{x} . Due to the Compton formula, we have a relation of the first scattering angle ω_1 and the energy of a photon after the first scattering event:

$$E_1 := \frac{E_0}{1 + \frac{E_0}{m_e c^2} (1 - \cos \omega_1)}. \quad (19)$$

Analogously, we compute the energy of a photon that arrives at the second scattering site \mathbf{y} with energy E_1 and is scattered in an angle ω_2 :

$$E_2 := \frac{E_1}{1 + \frac{E_1}{m_e c^2} (1 - \cos \omega_2)}. \quad (20)$$

We assume furthermore that the photon underlies no scattering process after that and is measured at \mathbf{d} with energy $E := E_2$, see figure 2.4. Then eq. (19) and eq. (20) together yield the relation

$$\cos \omega_1 + \cos \omega_2 = 2 - m_e c^2 \left(\frac{1}{E} - \frac{1}{E_0} \right) =: \lambda(E) \in (0, 2) \quad (21)$$

We obtain a representation of the second scattering angle in terms of the first angle:

$$\omega_2(\omega_1) = \arccos(\lambda(E) - \cos(\omega_1)) \quad (22)$$

We now want to derive an exact representation of the second scattering site \mathbf{y} in dependence on the first site \mathbf{x} , the first scattering angle ω_1 and the detected energy E at \mathbf{d} .

Lemma 1

Given the source \mathbf{s} , a detector \mathbf{d} , the measured photon energy E and a first scattering point \mathbf{x} with

scattering angle ω_1 , we can compute the second scattering point to be

$$\mathbf{y} = \mathbf{x} + r \begin{pmatrix} \sin(\omega_1 - \beta + \pi/2) \\ \cos(\omega_1 - \beta + \pi/2) \end{pmatrix} \quad \text{if } r > 0 \quad (23)$$

where the distance r between \mathbf{x} and \mathbf{y} is given by

$$r = \|\mathbf{d} - \mathbf{x}\| \left(\eta_2 - \cot(\omega_2(\omega_1)) \sqrt{1 - (\eta_2)^2} \right). \quad (24)$$

Hereby, the number η_2 is the second component of the vector

$$\eta := R^T \begin{pmatrix} \sin(\omega_1 - \beta + \pi/2) \\ \cos(\omega_1 - \beta + \pi/2) \end{pmatrix},$$

R is the orthogonal rotation matrix mapping $(0, 1)^T$ to $(\mathbf{d} - \mathbf{x}) / \|\mathbf{d} - \mathbf{x}\|$ and β is characterized by $\frac{\mathbf{x} - \mathbf{s}}{\|\mathbf{x} - \mathbf{s}\|} = (\cos \beta, \sin \beta)^T$.

Proof. See Appendix. □

A special case mentioned only indirectly in Lemma 1 is when the distance between \mathbf{x} and \mathbf{y} is computed to be $r \leq 0$, as the definition of \mathbf{y} was only given for positive r .

Start by considering $r = 0$: In this case, the first and second scattering site are computed to be the same point. In fact, by construction, the cone and the circular arcs always intersect at the point \mathbf{x} itself. The last case $r < 0$ actually corresponds to ω_1 being too large, meaning that the photons energy would have reduced to $E_1 < E$ after the first scattering. There cannot exist a second scattering point and the case is also ruled out. Indeed, the proof implicitly uses $r > 0$ at one point and for stability reasons, our numerical model will in fact assume that no second scattering can occur in a small neighbourhood $\mathfrak{N}(\mathbf{x})$ of the first site, by just restricting $r > \varepsilon$ with a small $\varepsilon > 0$.

We can now give a representation for the number of photons measured at the detector site using the previously computed relations:

Theorem 2

Assume we have a scanning architecture with a monochromatic, isotropic point source \mathbf{s} , a point detector at \mathbf{d} and the electron density $n_e(\mathbf{x})$ is compactly supported on $\Omega \subset \mathbb{R}^2$. Then the number of detected photons that are scattered exactly twice before being measured with an energy E , i.e. $g_2(E, \mathbf{d}, \mathbf{s})$, is proportional to the value

$$\mathcal{T}_2(n_e)(E, \mathbf{d}, \mathbf{s}) = \int_{\Omega} \int_{-\pi}^{\pi} w_2(\mathbf{x}, \omega_1; \mathbf{d}, \mathbf{s}) n_e(\mathbf{x}) n_e(\mathbf{y}(\omega_1)) dl(\omega_1) d\mathbf{x} \quad (25)$$

with the weight function

$$w_2(\mathbf{x}, \omega_1; \mathbf{d}, \mathbf{s}) = P(\omega_1) P(\omega_2(\omega_1)) A_{E_0}(\mathbf{s}, \mathbf{x}) A_{E_1}(\mathbf{x}, \mathbf{y}(\omega_1)) A_{E_2}(\mathbf{y}(\omega_1), \mathbf{d})$$

and the differential line segment

$$dl(\omega_1) = \sqrt{r^2 + \left(\frac{\partial r}{\partial \omega_1} \right)^2} d\omega_1.$$

where r is given in the previous Lemma.

Proof. See Appendix. □

Finally, we want to derive an alternative representation of \mathcal{T}_2 relating a measured energy E to an integral over the whole domain Ω^2 using a suited phase function.

Actually, in the case of \mathcal{T}_2 , we have to define the integration domain more carefully. As remarked after Lemma 1, we discard the degenerate case $\mathbf{y} = \mathbf{x}$ as it belongs actually to the first order scattering. Furthermore, we want to omit also all other cases in which the points \mathbf{s}, \mathbf{x} and \mathbf{y} lie on the same line. These correspond to the first scattering angle being either 0 or π , the first naturally being omitted as mentioned in the proof of Theorem 2. Leaving out also the latter case will be necessary to prove the mapping properties of \mathcal{T}_2 as an FIO and is not problematic in reality, as such a large scattering angle leads to very low photon energies that are outside the measured range anyway.

We therefore define

$$\Omega_2 := \{(\mathbf{x}, \mathbf{y}) \in \Omega^2 \mid \mathbf{y} - \mathbf{x} \neq \lambda(\mathbf{x} - \mathbf{s}) \text{ for any } \lambda \in \mathbb{R}\}. \quad (26)$$

In order to obtain the phase function, we represent the scattering angles in terms of the points $\mathbf{s}, \mathbf{x}, \mathbf{y}$ and \mathbf{d} . It holds

$$\cos \omega_1 = \kappa(\mathbf{y} - \mathbf{x}, \mathbf{x} - \mathbf{s}) = \frac{(\mathbf{y} - \mathbf{x})^T(\mathbf{x} - \mathbf{s})}{\|\mathbf{y} - \mathbf{x}\| \|\mathbf{x} - \mathbf{s}\|}$$

and, revisiting the characteristic function of the circular arcs from subsection 2.2,

$$\omega_2 = \cot^{-1}(\phi(\mathbf{y} - \mathbf{x}, \mathbf{d} - \mathbf{x}))$$

with $\phi = (\kappa - \rho)/\sqrt{1 - \kappa^2}$. Using the relation (21) between the scattering angles and the measured energy, we obtain that a combination of points $\mathbf{s}, \mathbf{x}, \mathbf{y}, \mathbf{d}$ yields a fixed energy E if and only if

$$\lambda(E) = \psi(\mathbf{y} - \mathbf{x}, \mathbf{x} - \mathbf{s}, \mathbf{d} - \mathbf{x}) := \kappa(\mathbf{y} - \mathbf{x}, \mathbf{x} - \mathbf{s}) + \cos(\cot^{-1}(\phi(\mathbf{y} - \mathbf{x}, \mathbf{d} - \mathbf{x}))).$$

We can therefore rewrite the operator \mathcal{T}_2 as

$$\mathcal{T}_2(n_e)(E, \mathbf{d}, \mathbf{s}) = \int_{\Omega_2} \mathcal{W}_2(n_e)(\mathbf{x}, \mathbf{y}, \mathbf{d}, \mathbf{s}) n_e(\mathbf{x}) n_e(\mathbf{y}) \delta(\lambda(E) - \psi(\mathbf{y} - \mathbf{x}, \mathbf{x} - \mathbf{s}, \mathbf{d} - \mathbf{x})) d\mathbf{x} d\mathbf{y}. \quad (27)$$

with the weight function $\mathcal{W}_2(n_e)(\mathbf{x}, \mathbf{y}, \mathbf{d}, \mathbf{s}) = \|\nabla_{\mathbf{x}, \mathbf{y}} \psi\| w_2(\mathbf{x}, \omega_1; \mathbf{d}, \mathbf{s})$.

2.4 Mapping Properties

One of the main ideas of the image reconstruction technique in this work arises from the properties of the previously established operators. As a motivation, consider an object n_e^{test} consisting only of two small, single disks in the plane. The measured number of first and second order scattered photons can be simulated by evaluating the operators \mathcal{T}_1 and \mathcal{T}_2 of this object for a fixed source \mathbf{s} and several detectors \mathbf{d} and energies E . The data is visualized in figure 2.5. Significant differences between $g_1 = \mathcal{T}_1 n_e^{\text{test}}$ and $g_2 = \mathcal{T}_2 n_e^{\text{test}}$ immediately become visible. The second order scattered data is more 'spread out' over the different energy levels and seems to be smoother in general.

Indeed, the goal of this section is to establish continuity results for the operators in the Sobolev spaces H^ν . Due to the complexity of the nonlinear operators \mathcal{T}_1 and \mathcal{T}_2 , they will first be approximated by linear counterparts $\mathcal{L}_1, \mathcal{L}_2$. Reshaping these, we prove that they are in fact Fourier integral operators (FIO) and use theory from [9, 13] to prove the Sobolev mapping properties. The motivation of \mathcal{L}_2 smoothing further than \mathcal{L}_1 while the latter better preserves the object's singularities reflects in these mapping properties.

Definition 3 (Linearization of \mathcal{T}_1)

Assume there is a smooth prior information $\tilde{n}_e \in C^\infty(\Omega)$ given which approximates the sought-for image. As a linear approximation of the first operator \mathcal{T}_1 , we define

$$\mathcal{L}_1^{\tilde{n}_e}(f)(p, \mathbf{s}, \mathbf{d}) = \int_{\Omega} \mathcal{W}_1(\tilde{n}_e)(\mathbf{x}, \mathbf{d}, \mathbf{s}) f(\mathbf{x}) \delta(p - \phi(\mathbf{x} - \mathbf{s}, \mathbf{d} - \mathbf{s})) d\mathbf{x} \quad (28)$$

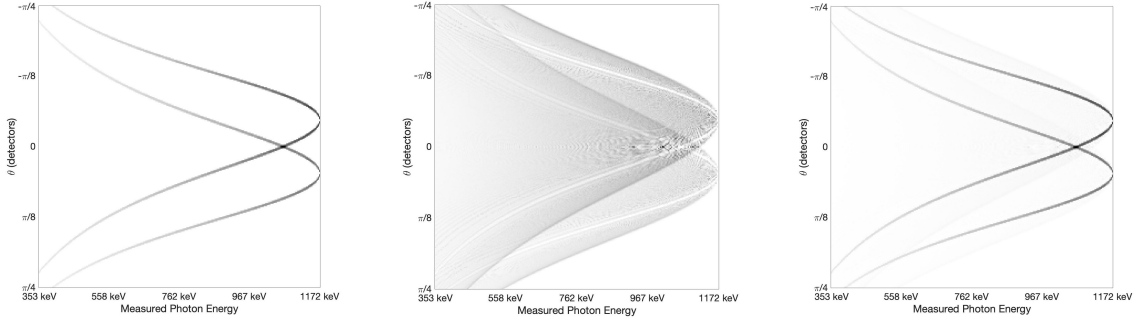


Figure 2.5: The data of an object consisting of two small disks in the plane. Left: only g_1 . Middle: Only g_2 . Right: $g_1 + g_2$.

where the only difference to \mathcal{T}_1 lies in the weight function $w_1 = \mathcal{W}_1(\tilde{n}_e)$ depending not on the function f , but rather on the prior.

Note that the first argument is now $p = \cot \omega$ instead of the energy E_ω . This simplifies notation and is not problematic since the three parameters p, ω and E are all related by bijective mappings.

Definition 4 (Linearization of \mathcal{T}_2)

Similarly, we define the linear operator $\mathcal{L}_2^{\tilde{n}_e}$ for a prior $\tilde{n}_e \in C^\infty(\Omega)$. To shorten the notation, the variables (\mathbf{x}, \mathbf{y}) are gathered as $\mathbf{z} := (\mathbf{x}, \mathbf{y}) \in \Omega_2 \subset \mathbb{R}^4$ and we denote $f(\mathbf{z}) := f(\mathbf{x})f(\mathbf{y})$ when f is applied to four-dimensional arguments. This yields

$$\mathcal{L}_2^{\tilde{n}_e}(f)(\lambda, \mathbf{s}, \mathbf{d}) = \int_{\Omega_2} \mathcal{W}_2(\tilde{n}_e)(\mathbf{x}, \mathbf{y}, \mathbf{d}, \mathbf{s}) f(\mathbf{z}) \delta(\lambda - \psi(\mathbf{y} - \mathbf{x}, \mathbf{x} - \mathbf{s}, \mathbf{d} - \mathbf{x})) d\mathbf{z}$$

where $\lambda = \lambda(E)$ as before.

Next, we want to examine the properties of \mathcal{L}_1 and \mathcal{L}_2 as FIOs. Therefore, we first recall definitions of the necessary terms as in [13, 9].

For a function $f : \mathbb{R}^n \rightarrow \mathbb{R}$, write

$$\partial_x f(x) = \sum_{i=1}^n \frac{\partial f}{\partial x_i} dx_i.$$

Further, we write $H_c^\nu(\Omega)$ for the space of all $u \in L^2(\Omega)$ compactly supported in Ω that satisfy

$$\|u\|_{H^\nu} = \left(\int_{\Omega} (1 + \|\xi\|^2)^\nu \|\hat{u}(\xi)\|^2 d\xi \right)^{1/2} < \infty$$

where \hat{u} is the Fourier transform of u and $H_{\text{loc}}^\nu(\Omega)$ for the space of all u supported in Ω such that $\chi u \in H_c^\nu(\Omega)$ for all compactly supported $\chi \in C_c^\infty(\Omega)$.

Definition 5 (Phase function, [13])

Let $Y \subset \mathbb{R}^m$ and $X \subset \mathbb{R}^n$ be open. Then the function $\Phi \in C^\infty(Y \times X \times \mathbb{R} \setminus \{0\})$ is called phase function if

- it is positively homogeneous of order 1 in the third argument and
- $(\partial_y \Phi, \partial_\sigma \Phi)$ and $(\partial_x \Phi, \partial_\sigma \Phi)$ never vanish for any $(y, x, \sigma) \in Y \times X \times \mathbb{R} \setminus \{0\}$.

The phase function is further called non-degenerate if $\partial_{y,x}(\partial_\sigma \Phi)$ do not vanish for $(y, x, \sigma) \in \Sigma_\Phi$ where

$$\Sigma_\Phi := \{(y, x, \sigma) \in Y \times X \times \mathbb{R} \setminus \{0\} \mid \partial_\sigma \Phi = 0\}.$$

Definition 6 (Fourier Integral Operator, [13])

The operator \mathcal{T} is called a Fourier integral operator of order $s - \frac{n+m-2}{4}$ if

$$\mathcal{T}f(y) = \int e^{i\Phi(y,x,\sigma)} p(y,x,\sigma) f(x) dx d\sigma, \quad (29)$$

where Φ is a non-degenerate phase function and the following property is satisfied:

For the function $p \in C^\infty(Y, X, \mathbb{R})$, called symbol of order s , it holds that, for every $K \subset Y \times X$ and all $\alpha \in \mathbb{N}_0, \beta \in \mathbb{N}_0^n, \gamma \in \mathbb{N}_0^m$, there exists a constant $C = C(K, \alpha, \beta, \gamma)$ such that

$$|D_\sigma^\alpha D_x^\beta D_y^\gamma p(y, x, \sigma)| \leq C(1 + \|\sigma\|)^{s-\alpha} \text{ for all } (y, x) \in K \text{ and } \sigma \in \mathbb{R}.$$

Lemma 7 ([9])

Consider the special case where $y = (p, \theta) \in \mathbb{R} \times \Theta =: Y$ with $\Theta \subset \mathbb{R}^{m-1}$ open and the phase function is of the form

$$\Phi(p, \theta, x, \sigma) = -\sigma(p - \phi(x, \theta)).$$

If the vectors $\nabla_x \phi, \partial_{\theta_1} \nabla_x \phi, \dots, \partial_{\theta_{m-1}} \nabla_x \phi$ are linearly independent for all $(p, \theta, x) \in \mathbb{R} \times \Theta \times X$, then

$$\mathcal{T} : H_c^\nu(X) \rightarrow H_{\text{loc}}^{\nu-k}(Y)$$

is a continuous operator.

It has been shown that FIOs are a useful tool when studying Radon transforms and generalized Radon transforms [13, 29, 8, 14]. We want to apply the theory to the attenuated circular Radon transforms \mathcal{L}_1 and \mathcal{L}_2 examined in this work.

We begin with \mathcal{L}_1 and rewrite it to fit the definition of an FIO. Using the Fourier transform of the Dirac delta, we obtain from eq. (28) the representation

$$\mathcal{L}_1^{\tilde{n}_e}(f)(p, \mathbf{s}, \mathbf{d}) = \frac{1}{2\pi} \int_\Omega \int_{\mathbb{R}} \mathcal{W}_1(\tilde{n}_e)(\mathbf{x}, \mathbf{d}, \mathbf{s}) n_e(\mathbf{x}) e^{-i\sigma(p - \phi(\mathbf{x} - \mathbf{s}, \mathbf{d} - \mathbf{s}))} d\sigma d\mathbf{x}.$$

In particular, the phase function $\Phi(p, \theta, \mathbf{x}, \sigma) = -\sigma(p - \phi(\mathbf{x} - \mathbf{s}, \mathbf{d}(\theta) - \mathbf{s}))$ is of the special form of Lemma 7, which shows that it is applicable to prove the Sobolev mapping property of \mathcal{L}_1 if all the necessary conditions are satisfied.

Theorem 8

Assume that $\tilde{n}_e \in C^\infty(\Omega)$ and that the source $\mathbf{s} \notin \Omega$ is fixed. Then the operator $\mathcal{L}_1^{\tilde{n}_e}$ is an FIO of order $-\frac{1}{2}$.

Proof. The proof consists in the verification of the different properties of the symbol and the phase function. For the details see the Appendix. \square

Given that \mathcal{L}_1 is an FIO, it remains to show the mapping property on a Sobolev space scale. For this, we first prove a Lemma which relates the main condition of Lemma 7, namely the linear independence of $\nabla_x \phi, \partial_\theta \nabla_x \phi$, to an equivalent condition on the measure geometry.

Lemma 9

Let the detectors be defined by

$$\mathbf{d}(\theta) = \mathbf{s} + t(\theta) \begin{pmatrix} \cos \theta \\ \sin \theta \end{pmatrix} \quad (30)$$

where $\theta \in \Theta$, Θ some open interval. Then, if we write $\mathbf{x} - \mathbf{s} = (r \cos \xi, r \sin \xi)^T$ and the condition

$$r \neq t(\theta) \cos(\theta - \xi) - t'(\theta) \sin(\theta - \xi) \quad (31)$$

is satisfied for all $\mathbf{x} \in \Omega$ and every $\theta \in \Theta$, we have that $\det(\nabla_x \phi, \partial_\theta \nabla_x \phi) \neq 0$ for all $(x, d) \in \Omega \times \mathbb{D}$.

Proof. See Appendix. \square

Having established condition (31) for the Sobolev mapping property, we can directly compute that it is satisfied for the scanning geometry we chose for our model in the subsection 2.1.

Theorem 10

Let $\tilde{n}_e \in C^\infty(\Omega)$. Let the detectors $\mathbf{d}(\theta)$ be spread on the circle S^1 , the source \mathbf{s} positioned somewhere on the circle, e.g. at $(-1, 0)^T$ and let the object be supported in the open disk of radius 1 around 0, i.e. $\Omega \subset B_1(0)$. Then the operator

$$\mathcal{L}_1^{\tilde{n}_e} : H_c^\nu(\Omega) \rightarrow H_{\text{loc}}^{\nu+1/2}(\mathbb{R} \times S^1)$$

is continuous.

Proof. The positions of the detectors relative to the source are given by

$$\mathbf{d}(\theta) = \mathbf{s} + 2 \cos \theta \begin{pmatrix} \cos \theta \\ \sin \theta \end{pmatrix},$$

where $t(\theta) = 2 \cos \theta$ and $\theta \in (-\pi/2, \pi/2)$. The preceding Lemma 9 together with Lemma 7 prove the theorem if eq. (31) is satisfied for all $\mathbf{x} - \mathbf{s} = (r \cos \xi, r \sin \xi) \in \Omega$. The condition reads

$$r \neq t(\theta) \cos(\theta - \xi) - t'(\theta) \sin(\theta - \xi) = 2 \cos \xi,$$

leading to $\mathbf{x} \notin S^1$, which is true due to the assumption $\Omega \subset B_1(0)$. □

This concludes our study of \mathcal{L}_1 . We now want to derive similar results for the second operator \mathcal{L}_2 . For this, start again by rewriting the integral transform in the form of an FIO:

$$\mathcal{L}_2^{\tilde{n}_e}(f)(\lambda, \mathbf{s}, \mathbf{d}) = \frac{1}{2\pi} \int_{\Omega_2} \mathcal{W}_2(\tilde{n}_e)(\mathbf{x}, \mathbf{y}, \mathbf{d}, \mathbf{s}) f(\mathbf{z}) e^{-i\sigma(\lambda - \psi(\mathbf{y} - \mathbf{x}, \mathbf{x} - \mathbf{s}, \mathbf{d} - \mathbf{x}))} d\sigma d\mathbf{z}$$

where we used again the Fourier representation of δ .

The phase is given by

$$\Psi(\lambda, \theta, \mathbf{x}, \mathbf{y}, \sigma) = -\sigma(\lambda - \psi(\mathbf{y} - \mathbf{x}, \mathbf{x} - \mathbf{s}, \mathbf{d}(\theta) - \mathbf{x}))$$

in the form of Lemma 7.

Theorem 11

Assume that $\tilde{n}_e \in C^\infty(\Omega)$. The operator $\mathcal{L}_2^{\tilde{n}_e}$ is an FIO of order -1 .

Proof. As for $\mathcal{L}_1^{\tilde{n}_e}$, the proof consists in computing the properties of the symbol and the phase. This is straightforward, but rather technical, and therefore moved to the Appendix. □

The corresponding Sobolev mapping property can now be proved in the same scanning geometry as before. Note that $\mathcal{L}_2^{\tilde{n}_e}$ maps half a step more on the Sobolev space scale than $\mathcal{L}_1^{\tilde{n}_e}$ when applied to the same function. This incorporates the core idea of the method, namely that g_2 is smoother than g_1 .

Theorem 12

Let $\tilde{n}_e \in C^\infty(\Omega)$ and the measure geometry be defined as in Theorem 10 - the detectors $\mathbf{d}(\theta)$ are distributed on S^1 , \mathbf{s} is fixed at $(-1, 0)$ and $\Omega \subset B_1(0)$. Then the operator

$$\mathcal{L}_2 : H_c^\nu(\Omega_2) \rightarrow H_{\text{loc}}^{\nu+1}((0, 2) \times S^1)$$

is continuous.

Proof. See Appendix. □

This concludes our analytic study of the operators. Although we only examined \mathcal{T}_1 and \mathcal{T}_2 here, the general idea can be extended further, as the emitted photons can of course scatter more often than two times in the object. Modeling the process of n scattering events would most probably be very complicated and proving suitable mapping properties for the arising operators even harder. Nevertheless, going out from our study of the first and second order here, one can expect that, in terms of the Sobolev mapping properties elaborated in Theorems 10 and 12, the higher order parts of the spectrum are contained at least in $H^1(Y)$ where $Y \subset \mathbb{R} \times \Theta$ as is g_2 , if not even in a Sobolev space $H^k(Y)$ with $k > 1$.

We are going to make use of the smoothness properties in the next section, where we derive a method to recover the image from the spectrum.

3 Image reconstruction combining smoothness properties and variational regularization

We now know how to model the parts g_1 and g_2 of the spectrum, have defined the corresponding forward operators \mathcal{T}_1 and \mathcal{T}_2 and their linearizations $\mathcal{L}_1^{\tilde{n}_e}$ and $\mathcal{L}_2^{\tilde{n}_e}$ using the prior image \tilde{n}_e from sparse CT. As section 2 showed, the task to recover f from the spectrum is an ill-posed problem. One elegant way to solve inverse problems defined by integral transforms are inversion formulae, a prominent example being the filtered backprojection algorithm in CT arising from the inversion formula of the Radon transform. Concerning the inversion of \mathcal{T}_1 , efforts have been made to reconstruct images from the projection data [23, 26, 3, 22], although often the physical factors are neglected in order to preserve linearity of the operator. Unfortunately, up to our best knowledge, an inversion for the operator \mathcal{T}_2 is not known, reasons for this are the complex structure of the phase function and also the nonlinearity of the operator.

In this work, we focus on an algebraic approach, constructing essentially a linear system of equations to recover the image from the spectrum. The forward model will hereby be a matrix representation of the linearized first order operator $\mathcal{L}_1^{\tilde{n}_e}$ using the prior \tilde{n}_e obtained from a CT step given g_0 . We check first that the forward operator is accurate enough to reconstruct the object n_e from the data given by $g_1 = \mathcal{T}_1(n_e)$.

After that, we include also the higher order terms and noise and try to reconstruct the object given the spectrum of scattered data

$$\mathfrak{S}(n_e) - g_0 = g_1 + g_2 + \eta$$

instead of g_1 only. The forward operator still being $\mathcal{L}_1^{\tilde{n}_e}$, we have to preprocess the spectrum. The main idea arising here is to differentiate the spectrum with respect to the energy, as we showed in the last section that the higher-order terms can be assumed smoother than g_1 .

In section 2.1 we have worked out a way to use the primary radiation g_0 to obtain a suited prior approximation \tilde{n}_e to the electron density of the object. The prior allowed to define the linear approximations $\mathcal{L}_1^{\tilde{n}_e}$ and $\mathcal{L}_2^{\tilde{n}_e}$ to the operators \mathcal{T}_1 and \mathcal{T}_2 modeling the spectrum $\mathfrak{S}(n_e)$.

We have to check now whether the prior is sufficient to approximate the forward operator \mathcal{T}_1 by the linearized version $\mathcal{L}_1^{\tilde{n}_e}$. We therefore aim to solve first the inverse problem

$$\text{Find } f \text{ such that } \mathcal{L}_1^{\tilde{n}_e}(f) = \mathcal{T}_1(n_e^{\text{ex}}), \quad (32)$$

We reformulate the problem as a minimization task. Let $g_1 := \mathcal{T}_1(n_e^{\text{ex}})$ be the data obtained from the exact forward operator. Given \tilde{n}_e , we solve the problem

$$n_e^\lambda = \arg \min_f \left\| \mathcal{L}_1^{\tilde{n}_e} f - g_1 \right\|_2^2 + \lambda J_\beta(f) \quad (33)$$

where J_β is a penalty function and $\lambda > 0$ a regularization parameter.

Typically, a choice for J_β should enhance favorable properties of the image like low variation or low L^1 -norm. Prominent choices are therefore e.g. the L^1 -norm, the BV-norm or the BV-seminorm, also referred to as total variation. Here we choose the functional J_β to be a differentiable approximation of the total variation $\text{TV}(f)$ defined by

$$J_\beta(f) := \sup \left\{ \int_{\Omega} \left(-f \operatorname{div} h + \sqrt{\beta(1 - |h(x)|^2)} \right) dx \mid h \in C_0^1(\Omega, \mathbb{R}^n) : |h(x)| \leq 1 \ \forall x \in \Omega \right\}$$

with $\beta > 0$ small. It holds $J_0(f) = \text{TV}(f)$ and it can be easily proved that J_β generalizes the total variation $\text{TV}(f)$ in a very natural way, in the sense that

$$J_\beta(f) = \int_{\Omega} \sqrt{|\nabla f|^2 + \beta} \, dx \quad (34)$$

if $f \in W^{1,1}(\Omega)$, where $W^{1,1}(\Omega)$ is the Sobolev space of weakly differentiable functions in $L^1(\Omega)$. For more informations on the existence and uniqueness of solutions to 33, see [1].

The scanning geometry stays unchanged, in particular we compute the data $g_1 = \mathcal{T}_1 n_e^{\text{ex}}$ for 16 source positions with 32 detectors each. The source is assumed to emit monochromatic photons at 1.173 MeV and the detectors measure 256 different energy levels, distributed equidistantly in the range from 0.355 MeV to 1.173 MeV. The necessary energy resolution in the detector is therefore $\Delta E \approx 3.2$ keV. The data g_1 is visualized in figure 3.1a for a single source and in 3.1b for all 16 sources at once.

Due to the large dimension of the linear system, we solve the problem (33) by a nonlinear conjugate gradient method using the Fletcher-Reeves rule for the update of the search direction and a realization of the strong Wolfe-Powell rule for the stepsize computation. See [6] for a detailed study of the method. The results are depicted in figure 3.2a and 3.2b for $\lambda = 0$ and $\lambda > 0$ tuned empirically.

Although the CT step is not able to recover any detail and the prior image \tilde{n}_e we use is rather shadowy and inaccurate, see figure 2.2, it turns out that it is sufficiently good to recover a very good approximation to n_e^{ex} from the minimization problem (33).

Up next, we can try and apply the exact same method to the problem

$$n_e^\lambda = \arg \min_f \left\| \mathcal{L}_1^{\tilde{n}_e} f - (g_1 + g_2 + \eta) \right\|_2^2 + \lambda J_\beta(f), \quad (35)$$

where η is Poisson noise and the first and second order data is computed by

$$g_1 + g_2 = (\mathcal{T}_1 + \mathcal{T}_2)(n_e^{\text{ex}}).$$

Hereby, g_2 is computed in the same configuration as g_1 , the resulting data is visualized 3.1c and 3.1d. The sum of all three terms, $g_1 + g_2 + \eta$, is depicted in 3.1e and 3.1f. Applying the same nonlinear conjugate gradient method as before, we obtain the results shown in figure 3.2c and 3.2d.

We immediately see that the incorporation of the whole scattered spectrum makes a reconstruction from $\mathcal{L}_1^{\tilde{n}_e}$ alone impossible when $\lambda = 0$ (middle image). This is not surprising as we now actually tried to solve the inverse problem

$$\text{Find } f \text{ such that } \mathcal{L}_1^{\tilde{n}_e}(f) = (\mathcal{T}_1 + \mathcal{T}_2)(n_e^{\text{ex}}) + \eta, \quad (36)$$

where the forward operator does not model a large part of the data, namely $g_2 + \eta$. One could try and increase the parameter λ controlling the total variation to very large values in order to force the variation to stay low, but this makes small details or lower-contrast regions in the object disappear as well, see the image on the right in 3.2d.

Instead of viewing g_2 and η both as plain noise and tackling this noise by regularization in the reconstruction process itself, we hope to reduce the artifacts by exploiting the structure of this

'noise'. When proving the mapping properties of the FIOs in section 2.4, we already discussed the notion of g_2 being smoother than g_1 in terms of Sobolev spaces. We propose to apply another operator \mathcal{D} to the data, transforming (36) to the inverse problem

$$\text{Find } f \text{ such that } \mathcal{D}\mathcal{L}_1^{\tilde{n}_e}(f) = \mathcal{D}((\mathcal{T}_1 + \mathcal{T}_2)(n_e^{\text{ex}}) + \eta), \quad (37)$$

\mathcal{D} must be chosen carefully as it should not increase the ill-posedness or ill-conditioning of the problem too much and preserve important information about the object in g_1 . At the same time, it should reduce as much as possible the impact of g_2 on the reconstruction. Assuming $f \in L^2(\Omega)$, an optimal choice would satisfy

$$\text{im}(\mathcal{T}_2) \subset \ker(\mathcal{D}), \quad \text{im}(\mathcal{T}_1) \subset \ker(\mathcal{D})^\perp$$

and have favorable numerical properties, where im is the image of $L^2(\Omega)$ under the respective operator and \ker the null space. Note that these optimal properties are difficult to verify though as we have no exact representation of the images of $\mathcal{T}_1, \mathcal{T}_2$.

Motivated by the smoothness properties of g_2 over g_1 , we propose to choose \mathcal{D} a differential operator, in particular $\mathcal{D} = \partial_E$ where E is the energy variable. The hope behind this choice is that the magnitude of smooth parts in g_2 are reduced under the derivative. The differentiation step itself is ill-posed. As we apply it also to η , which can consist of noise with large variation, the derivative is regularized by a low pass filter function F_γ , $\gamma > 0$. This yields an operator \mathcal{D}^γ defined by

$$\mathcal{D}^\gamma g^{\text{s,d}} := \mathcal{F}^{-1}(i\zeta \cdot F_\gamma(\zeta) \cdot \mathcal{F}(g^{\text{s,d}})(\zeta)) \quad (38)$$

where $g^{\text{s,d}}$ is the restriction of the data to a given source-detector pair and \mathcal{F} is the Fourier transform w.r.t. the energy variable.

Incorporating \mathcal{D}^γ into the minimization formulation of our inverse problem, we obtain

$$n_e^\lambda = \arg \min_f \left\| \mathcal{D}^\gamma (\mathcal{L}_1^{\tilde{n}_e} f - (g_1 + g_2 + \eta)) \right\|_2^2 + \lambda J_\beta(f), \quad (39)$$

The nonlinear conjugate gradient method is applied to the problem and the recovered images shown in 3.2e and 3.2f. Using first $\lambda = 0$ for the left image, we can see that the noise in the data still distorts the image, but much less than in the case without the differential operator. Applying total variation regularization, we can rule out large parts of the persisting noise and obtain a better reconstruction of the phantom, see the image on the right. Although some artifacts are still visible, all the details of the original image are preserved.

4 Conclusion

In this paper we proposed a reconstruction strategy for two-dimensional objects based on a bimodality of Computerized Tomography and Compton Scattering Tomography. We consider a standard fan-beam geometry and assume the cameras are able to measure the energy spectrum of the incoming photons. Focusing on first-order and second-order scattering, we derived and studied operators describing the polychromatic spectrum. Linearizations of these operators were studied as examples of the general class of Fourier integral operators in order to prove suitable mapping properties. In particular, we proved that the second-order scattering behaves as a smoother mapping as the first-order scattering. Due to the complexity of the terms of higher order in the spectrum, we first restricted the inverse problem to the modeling of the first-order scattering, but this simple approach turned out to be unsatisfactory as the higher-order scattering bring a large distortion of the spectrum. However the mapping properties reveal that this distortion of the spectrum due to the multiple scattering is smoother in comparison with the first-order scattering. We thus exploited the structure of the spectrum by applying a differential operator to the data. The efficiency of the proposed algorithm was validated on synthetic data.

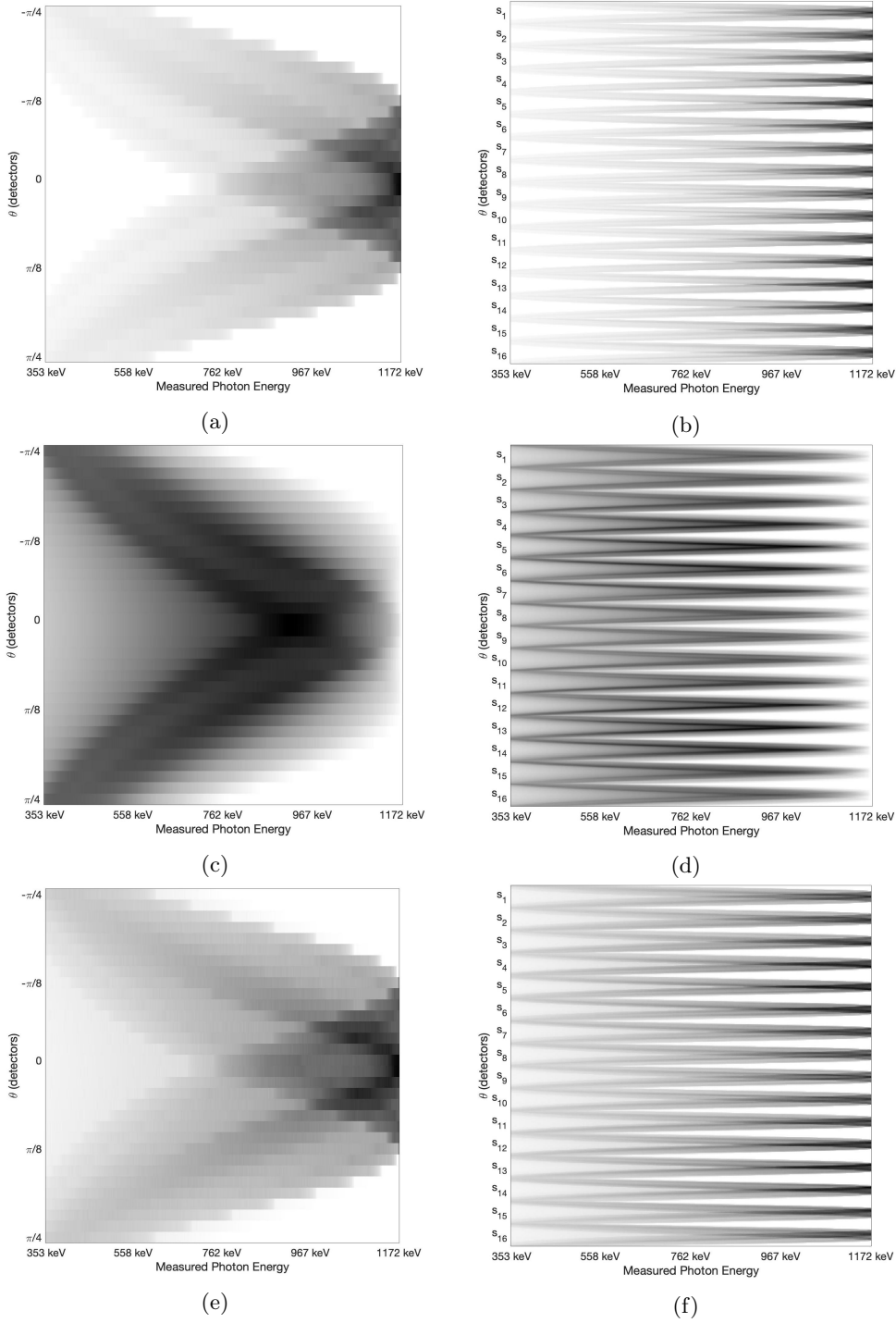


Figure 3.1: In the left column, the data for a single source is visualized. One source projects to 32 detectors, each detector measures 256 energy levels between 0.355 MeV and 1.173 MeV (energy resolution $\Delta E \approx 3.2$ keV). In the right column, the data for all 16 sources is depicted. The first row shows $g_1 = \mathcal{T}_1 n_e^{\text{ex}}$, the middle row $g_2 = \mathcal{T}_2 n_e^{\text{ex}}$ (note, at a different scale) and the last row our approximation to the spectrum $g_1 + g_2 + \eta$.

Acknowledgment

Gaël Rigaud is supported by the Deutsche Forschungsgemeinschaft (DFG) under the grant RI 2772/2-1.

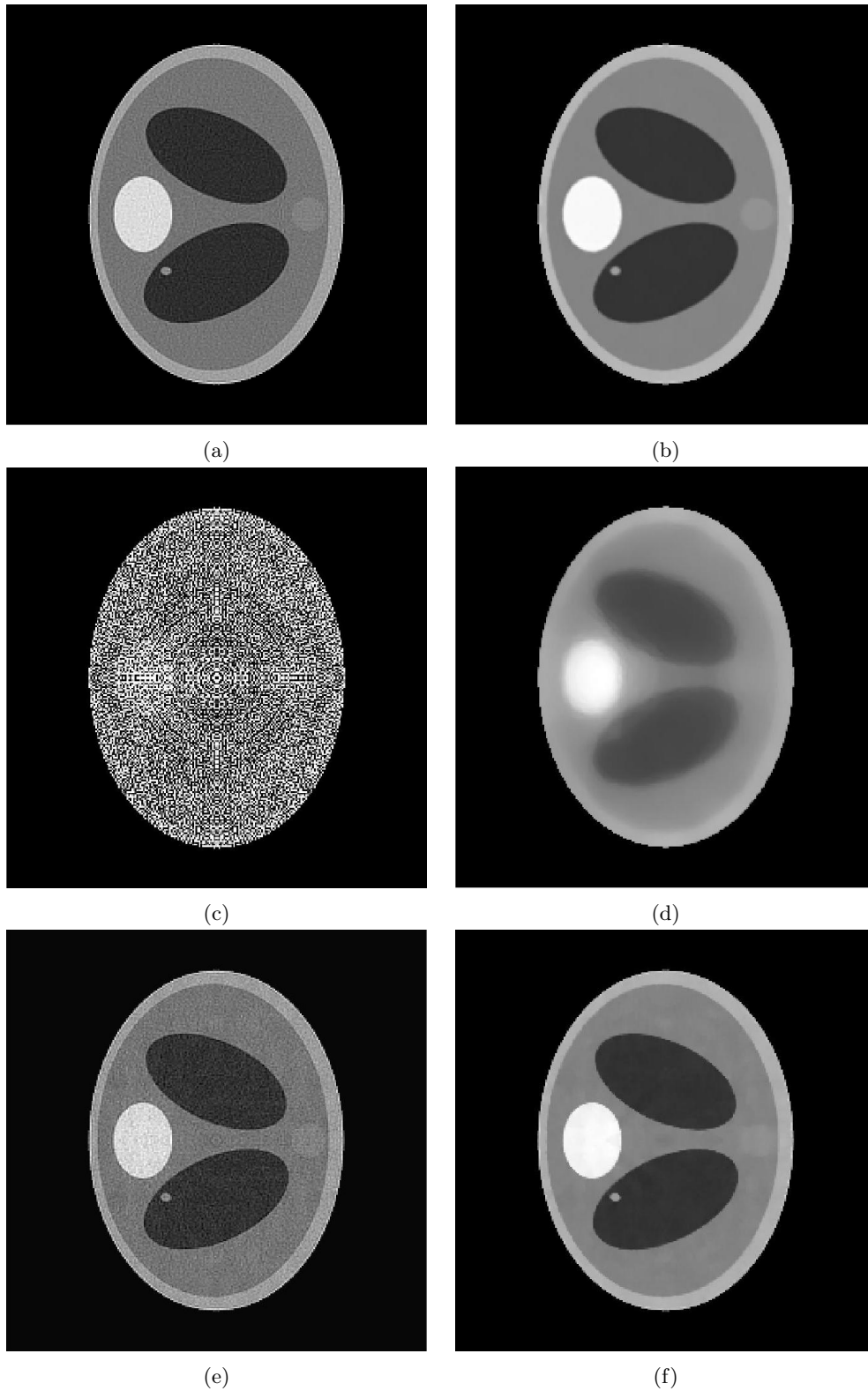


Figure 3.2: Left: Reconstructions without TV term. Right: $\lambda > 0$ tuned individually.
 Top row: Solutions of Problem 33 with data g_1 .
 Middle row: Solutions of Problem 35, the data is now the whole spectrum.
 Bottom row: Solutions of Problem 39, whole spectrum given, a differential operator is applied

Appendix

Proof of Lemma 1. After the photon is scattered at \mathbf{x} , its trajectory is a straight line that forms an angle of $\pi - \omega_1$ with the incoming beam direction $\mathbf{x} - \mathbf{s}$. Thus, its trajectory is part of the cone opening at \mathbf{x} with direction $\mathbf{x} - \mathbf{s}$ and aperture ω_1 . As we only consider the two-dimensional case, the cone simplifies to two possible directions, resembling the shape of a "V", see the dotted lines in figure 2.4. We simplify notation by introducing a convention of a signed angle ω_1 , restricting ω_1 not to $[0, \pi]$ but to $[-\pi, \pi]$, although both $\pm\omega_1$ yield the same energy E_1 after the first scatter event. The photon's trajectory after the first scattering is then a subset of the line

$$\mathcal{L}(\omega_1, \mathbf{x}, \mathbf{s}) = \left\{ \mathbf{x} + t \begin{pmatrix} \sin(\omega_1 - \beta + \pi/2) \\ \cos(\omega_1 - \beta + \pi/2) \end{pmatrix}, t \in \mathbb{R}^+ \right\} \quad (40)$$

with $\omega_1 \in [-\pi, \pi]$, where $\beta \in [0, 2\pi)$ is defined by $\frac{\mathbf{x}-\mathbf{s}}{\|\mathbf{x}-\mathbf{s}\|} = (\cos \beta, \sin \beta)^T$.

By (22) and fixing the measured energy E at \mathbf{d} , we already have an explicit representation for the second scattering angle $\omega_2(\omega_1)$. Interpreting \mathbf{x} as a radiation source, we know, equivalently as in the modeling of g_1 , that \mathbf{y} is a point on one of two symmetric circular arcs that can be parametrized by

$$\begin{aligned} \mathcal{C}(\omega_2, \mathbf{d}, \mathbf{x}) &= \left\{ \mathbf{x} + \|\mathbf{d} - \mathbf{x}\| \frac{\sin(\omega_2 - \alpha)}{\sin \omega_2} R \begin{pmatrix} \pm \sin \alpha \\ \cos \alpha \end{pmatrix}, \alpha \in [0, \omega_2] \right\} \\ &=: \left\{ \mathbf{x} + r(\omega_2, \alpha) d^\pm(\alpha), \alpha \in [0, \omega_2] \right\}. \end{aligned} \quad (41)$$

where R is an orthogonal rotation matrix mapping $(0, 1)^T$ to $(\mathbf{d} - \mathbf{x}) / \|\mathbf{d} - \mathbf{x}\|$ and the \pm -sign distinguishes the two separated circular arcs. The second formulation includes a unit vector $d^\pm(\alpha) := R(\pm \sin \alpha, \cos \alpha)^T$ and a corresponding scaling factor $r(\omega_2, \alpha) := \|\mathbf{d} - \mathbf{x}\| \sin(\omega_2 - \alpha) / \sin \omega_2$.

We can now compute the possible intersection points \mathbf{y} by comparing the parametrizations (40) and (41). Subtracting \mathbf{x} and applying R^{-1} , we obtain that

$$t\eta := tR^{-1} \begin{pmatrix} \sin(\omega_1 - \beta + \pi/2) \\ \cos(\omega_1 - \beta + \pi/2) \end{pmatrix} = r(\omega_2, \alpha) \begin{pmatrix} \pm \sin \alpha \\ \cos \alpha \end{pmatrix} \quad (42)$$

at an intersection point, hereby η only depends on the location of \mathbf{x} and \mathbf{d} . Further, it is well-defined and can be computed easily as $R^{-1} = R^T$, the second component is given by

$$\cos \alpha = \eta_2 = R_{1,2} \sin(\omega_1 - \beta + \pi/2) + R_{2,2} \cos(\omega_1 - \beta + \pi/2). \quad (43)$$

Using trigonometric identities, we can rewrite r only depending on the value of ω_2 and $\cos \alpha$, which allows to insert $\cos \alpha = \eta_2$:

$$\begin{aligned} r(\omega_2, \alpha) &= \|\mathbf{d} - \mathbf{x}\| \left(\cos \alpha - \cot \omega_2 \sqrt{1 - \cos^2 \alpha} \right) \\ &= \|\mathbf{d} - \mathbf{x}\| \left(\eta_2 - \cot \omega_2 \sqrt{1 - (\eta_2)^2} \right) =: r \end{aligned}$$

Inserting these values in the representation of \mathbf{y} yields the intersection point

$$\mathbf{y} = \mathbf{x} + r \begin{pmatrix} \sin(\omega_1 - \beta + \pi/2) \\ \cos(\omega_1 - \beta + \pi/2) \end{pmatrix} \quad \text{if } r > 0$$

of the circular arcs $\mathcal{C}(\omega_2, \mathbf{d}, \mathbf{x})$ with the line $\mathcal{L}(\omega_1, \mathbf{x}, \mathbf{s})$. □

Proof of Theorem 2. Similar to (15), but inserting a second scattering site and taking into account the physical factors, we can write for the variation of photons scattered twice at points \mathbf{x} and \mathbf{y}

$$d^2 N(\mathbf{s}, \mathbf{d}, \mathbf{x}, \mathbf{y}) = I_0 r_e^4 A_{E_0}(\mathbf{s}, \mathbf{x}) A_{E_1}(\mathbf{x}, \mathbf{y}) A_{E_2}(\mathbf{y}, \mathbf{d}) P(\omega_1) P(\omega_2) n_e(\mathbf{x}) n_e(\mathbf{y}) d\mathbf{x} d\mathbf{y}. \quad (44)$$

This relation is integrated over all possible first scattering sites \mathbf{x} . Fixing a measured energy E , one further integrates over all possible first scattering angles ω_1 . For every ω_1 , we can compute the corresponding $\omega_2(\omega_1)$ and the second scattering site $\mathbf{y}(\omega_1) \in \mathfrak{C}(\omega_2, \mathbf{d}, \mathbf{x}) \cap \mathfrak{L}(\omega_1, \mathbf{x}, \mathbf{s})$ by the previous Lemma 1. We obtain that g_2 is proportional to

$$\mathcal{T}_2(n_e)(E, \mathbf{d}, \mathbf{s}) = \int_{\Omega} \int_{(-\pi, \pi) \setminus \{0\}} w_2(\mathbf{x}, \omega_1; \mathbf{d}, \mathbf{s}) n_e(\mathbf{x}) n_e(\mathbf{y}(\omega_1)) dl(\omega_1) d\mathbf{x}$$

with the weight function w_2 as stated in the theorem and the differential line element $dl(\omega_1)$ encoding the change in the second scattering site \mathbf{y} by the first scattering angle. We remark here that of course $\omega_1 = 0$ is a zero set so it doesn't alter the value of the integral, but it corresponds to the case of no real scattering event and is therefore technically ruled out.

It remains to compute $dl(\omega_1) = \left\| \frac{\partial \mathbf{y}}{\partial \omega_1} \right\| d\omega_1$. For this, we define \tilde{R} to be an orthogonal matrix rotating by an angle $\omega_1 - \beta + \pi/2$ and see that

$$\begin{aligned} \frac{\partial \mathbf{y}}{\partial \omega_1} &= \frac{\partial}{\partial \omega_1} \left(\mathbf{x} + r \begin{pmatrix} \sin(\omega_1 - \beta + \pi/2) \\ \cos(\omega_1 - \beta + \pi/2) \end{pmatrix} \right) \\ &= \frac{\partial r}{\partial \omega_1} \begin{pmatrix} \sin(\omega_1 - \beta + \pi/2) \\ \cos(\omega_1 - \beta + \pi/2) \end{pmatrix} + r \begin{pmatrix} \cos(\omega_1 - \beta + \pi/2) \\ -\sin(\omega_1 - \beta + \pi/2) \end{pmatrix} \\ &= \frac{\partial r}{\partial \omega_1} \tilde{R} \begin{pmatrix} 0 \\ 1 \end{pmatrix} + r \tilde{R} \begin{pmatrix} 1 \\ 0 \end{pmatrix} = \tilde{R} \begin{pmatrix} r \\ \frac{\partial r}{\partial \omega_1} \end{pmatrix} \end{aligned}$$

from which we immediately conclude the identity $dl(\omega_1) = \sqrt{r^2 + \left(\frac{\partial r}{\partial \omega_1}\right)^2} d\omega_1$ where the derivative of r is given by

$$\frac{\partial r}{\partial \omega_1} = \frac{\partial \eta_2}{\partial \omega_1} \left(1 + \cot \omega_2 \frac{\eta_2}{\sqrt{1 - \eta_2^2}} \right) - \frac{\sin \omega_1}{\sin^3 \omega_2} \sqrt{1 - \eta_2^2}$$

with η_2 given by (43) and

$$\frac{\partial \eta_2}{\partial \omega_1} = R_{1,2} \cos(\omega_1 - \beta + \pi/2) - R_{2,2} \sin(\omega_1 - \beta + \pi/2)$$

□

Proof of Theorem 8. As \tilde{n}_e is C^∞ -smooth, so is the weight function $\mathcal{W}_1(\tilde{n}_e)(\mathbf{x}, \mathbf{d}, \mathbf{s})$. Further, the weight does not depend on σ at all, so it is immediately clear that it is a symbol of order 0.

We fix the source position \mathbf{s} and parametrize the detector position $\mathbf{d}(\theta)$ by $\theta \in \Theta$ where $\Theta \subset \mathbb{R}$ open. It remains to prove that $\Phi(p, \theta, \mathbf{x}, \sigma) = -\sigma(p - \phi(\mathbf{x} - \mathbf{s}, \mathbf{d}(\theta) - \mathbf{s}))$ is a non-degenerate phase function. The positive homogeneity is clear as Φ is linear in σ . It holds

$$\partial_{p, \theta} \Phi = -\sigma(dp - \partial_\theta \phi(\mathbf{x} - \mathbf{s}, \mathbf{d}(\theta) - \mathbf{s})) \neq 0$$

for every $(p, \theta, \mathbf{x}, \sigma) \in \mathbb{R} \times \Theta \times \Omega \times \mathbb{R} \setminus \{0\}$, in particular $(\partial_{p, \theta} \Phi, \partial_\sigma \Phi)$ doesn't vanish.

Furthermore, it holds $\partial_{\mathbf{x}} \Phi = \sigma \partial_{\mathbf{x}} \phi = 0$ if and only if $\nabla_{\mathbf{x}} \phi = 0$ as $\sigma \neq 0$. For the gradient, we obtain using the definition (16) of ϕ

$$\nabla_{\mathbf{x}} \phi(\mathbf{x} - \mathbf{s}, \mathbf{d} - \mathbf{s}) = \frac{1 - \rho \kappa}{\|\mathbf{x} - \mathbf{s}\| (1 - \kappa^2)^{3/2}} \left(\frac{\mathbf{d}(\theta) - \mathbf{s}}{\|\mathbf{d}(\theta) - \mathbf{s}\|} - \kappa \frac{\mathbf{x} - \mathbf{s}}{\|\mathbf{x} - \mathbf{s}\|} \right) - \frac{\rho}{\|\mathbf{x} - \mathbf{s}\| (1 - \kappa^2)^{1/2}} \frac{\mathbf{x} - \mathbf{s}}{\|\mathbf{x} - \mathbf{s}\|}.$$

The two vectors summed up are orthogonal by the definition of κ . Hereby, the component in the direction of $(\mathbf{x} - \mathbf{s})/\|\mathbf{x} - \mathbf{s}\| \neq 0$ is never zero as $\rho \neq 0$, so we have $\nabla_{\mathbf{x}} \phi \neq 0$ and ϕ is a phase function.

It remains to prove that the phase function is also non-degenerate. We have

$$\partial_\sigma \Phi = (\phi(\mathbf{x} - \mathbf{s}, \mathbf{d}(\theta) - \mathbf{s}) - p) d\sigma$$

and therefore

$$\partial_{\mathbf{x}, p, \theta}(\partial_\sigma \Phi) = (\partial_{\mathbf{x}} \phi + \partial_\theta \phi - dp) d\sigma \neq 0$$

so we have proved that $\mathcal{L}_1^{\tilde{n}_e}$ is indeed an FIO.

It holds $\Omega \subset \mathbb{R}^2$ open and $\Theta \subset \mathbb{R}$ open, i.e. $n = m = 2$. The symbol is of order 0, therefore $\mathcal{L}_1^{\tilde{n}_e}$ is an FIO of order

$$k = 0 - \frac{2 + 2 - 2}{4} = -\frac{1}{2}.$$

□

Proof of Lemma 9. Recall the definition of the examined function

$$\phi(\mathbf{x} - \mathbf{s}, \mathbf{d} - \mathbf{s}) = \frac{\kappa(\mathbf{x} - \mathbf{s}, \mathbf{d} - \mathbf{s}) - \rho(\mathbf{x} - \mathbf{s}, \mathbf{d} - \mathbf{s})}{\sqrt{1 - \kappa(\mathbf{x} - \mathbf{s}, \mathbf{d} - \mathbf{s})^2}}.$$

Shortening notation, we write $a := \mathbf{x} - \mathbf{s}$, $b := \mathbf{d} - \mathbf{s}$ and further $\kappa := \kappa(a, b)$, $\rho := \rho(a, b)$.

As in the proof of Theorem 8, we obtain for the gradient

$$\nabla_{\mathbf{x}} \phi(\mathbf{x} - \mathbf{s}, \mathbf{d} - \mathbf{s}) = \frac{1 - \rho\kappa}{\|a\| (1 - \kappa^2)^{3/2}} \left(\frac{b}{\|b\|} - \kappa \frac{a}{\|a\|} \right) - \frac{\rho}{\|a\| (1 - \kappa^2)^{1/2}} \frac{a}{\|a\|}.$$

At this point, we introduce a change of coordinates by applying the unique orthogonal rotation R_a that maps a to $(\|a\|, 0)^T$ in \mathbb{R}^2 . As R_a is a rotation and also independent of θ , it does not alter the examined determinant when applied to $\nabla_{\mathbf{x}} \phi$:

$$\det(\nabla_{\mathbf{x}} \phi, \partial_\theta \nabla_{\mathbf{x}} \phi) = \det(R_a \nabla_{\mathbf{x}} \phi, \partial_\theta R_a \nabla_{\mathbf{x}} \phi).$$

In the new coordinate system, using $R_a b = t(\theta)(\cos(\theta - \xi), \sin(\theta - \xi))^T$ and $\kappa = \cos(\theta - \xi)$ we can simplify the gradient to

$$R_a \nabla_{\mathbf{x}} \phi(\mathbf{x} - \mathbf{s}, \mathbf{d} - \mathbf{s}) = \frac{1}{t(\theta) |\sin(\theta - \xi)|} \begin{pmatrix} -1 \\ \frac{t(\theta)}{r \sin(\theta - \xi)} - \cot(\theta - \xi) \end{pmatrix}.$$

The vector can now be differentiated with respect to theta yielding

$$\partial_\theta R_a \nabla_{\mathbf{x}} \phi(\mathbf{x} - \mathbf{s}, \mathbf{d} - \mathbf{s}) = \frac{|\sin(\theta - \xi)|}{t(\theta) \sin^2(\theta - \xi)} \begin{pmatrix} \cot(\theta - \xi) + \frac{t'(\theta)}{t(\theta)} \\ \cot^2(\theta - \xi) + \frac{r - 2t(\theta) \cos(\theta - \xi)}{r \sin^2(\theta - \xi)} + \frac{t'(\theta)}{t(\theta)} \cot(\theta - \xi) \end{pmatrix}$$

which leads directly to the sought for determinant

$$\det(\nabla_{\mathbf{x}} \phi, \partial_\theta \nabla_{\mathbf{x}} \phi) = \frac{1}{rt(\theta)^2 \sin^4(\theta - \xi)} (t(\theta) \cos(\theta - \xi) - t'(\theta) \sin(\theta - \xi) - r).$$

Assuming condition (31) is true, the determinant never vanishes, which concludes the proof. □

Proof of Theorem 11. The weight function is, as for \mathcal{L}_1 , a symbol of order zero as it is C^∞ -smooth and does not depend on σ .

The phase function Ψ given by

$$\Psi(\lambda, \theta, \mathbf{x}, \mathbf{y}, \sigma) = -\sigma(\lambda - \psi(\mathbf{y} - \mathbf{x}, \mathbf{x} - \mathbf{s}, \mathbf{d}(\theta) - \mathbf{x}))$$

is in $C^\infty((0, 2) \times \Theta \times \Omega_2 \times \mathbb{R} \setminus \{0\})$ and obviously homogeneous of order 1 in σ .

We have to check that $(\partial_{\lambda,\theta}\Psi, \partial_\sigma\Psi)$ and $(\partial_{\mathbf{z}}\Psi, \partial_\sigma\Psi)$ do not vanish for $\sigma \neq 0$. We start with the easier first pair as it holds

$$\partial_{\lambda,\theta}\Psi = -\sigma(d\lambda - \partial_\theta\psi(\mathbf{y} - \mathbf{x}, \mathbf{x} - \mathbf{s}, \mathbf{d}(\theta) - \mathbf{x})) \neq 0$$

when $\sigma \neq 0$. Thus $(\partial_{\lambda,\theta}\Psi, \partial_\sigma\Psi)$ does not vanish.

The first two components of $\partial_{\mathbf{z}}\Psi$ are

$$\partial_{\mathbf{x}}\Psi = \sigma\partial_{\mathbf{x}}\psi(\mathbf{y} - \mathbf{x}, \mathbf{x} - \mathbf{s}, \mathbf{d}(\theta) - \mathbf{x})$$

which is zero if and only if $\nabla_{\mathbf{x}}\psi(\mathbf{y} - \mathbf{x}, \mathbf{x} - \mathbf{s}, \mathbf{d}(\theta) - \mathbf{x}) = 0$. Abbreviating $a := \mathbf{y} - \mathbf{x}$, $b := \mathbf{x} - \mathbf{s}$ and $c := \mathbf{d} - \mathbf{x}$, where $a, b, c \neq 0$, the gradient is given by

$$\nabla_{\mathbf{x}}(\psi(\mathbf{y} - \mathbf{x}, \mathbf{x} - \mathbf{s}, \mathbf{d} - \mathbf{x})) = (-\nabla_a + \nabla_b)\kappa(a, b) - \frac{1}{(1 + \phi(a, c)^2)^{3/2}}(\nabla_a + \nabla_c)\phi(a, c). \quad (45)$$

By straightforward differentiation by a and the symmetry $\kappa(a, b) = \kappa(b, a)$ we obtain

$$\begin{aligned} \nabla_a\kappa(a, b) &= \frac{b}{\|a\| \|b\|} - \frac{a \cdot b}{\|a\|^3 \|b\|} a \\ \nabla_b\kappa(a, b) &= \frac{a}{\|a\| \|b\|} - \frac{a \cdot b}{\|a\| \|b\|^3} b \end{aligned}$$

and, writing $\bar{\rho} = \rho(a, b) = \|a\| / \|b\|$ as well as $\bar{\kappa} = \kappa(a, b)$, their difference can be simplified to

$$(-\nabla_a + \nabla_b)\kappa(a, b) = (\bar{\kappa} + \bar{\rho}) \frac{a}{\|a\|^2} - (\bar{\kappa} + \bar{\rho}^{-1}) \frac{b}{\|b\|^2}. \quad (46)$$

Next, we compute the terms depending on (a, c) . Abbreviating $\kappa = \kappa(a, c)$, $\rho = \rho(a, c)$, we get

$$\begin{aligned} (1 + \phi(a, c)^2)^{-3/2} &= \left(1 + \left(\frac{\kappa - \rho}{1 - \kappa^2}\right)^2\right)^{3/2} = \left(\frac{1 - \kappa^2}{1 - 2\kappa\rho + \rho^2}\right)^{3/2}, \\ \nabla_a\phi(a, c) &= \frac{1}{\|a\| (1 - \kappa^2)^{3/2}} \left((-\kappa - \rho + 2\rho\kappa^2) \frac{a}{\|a\|} + (1 - \rho\kappa) \frac{c}{\|c\|} \right), \\ \nabla_c\phi(a, c) &= \frac{1}{\|c\| (1 - \kappa^2)^{3/2}} \left((1 - \rho\kappa) \frac{a}{\|a\|} - (\kappa - \rho) \frac{c}{\|c\|} \right). \end{aligned}$$

The combination of these three terms simplifies then to

$$-\frac{1}{(1 + \phi(a, c)^2)^{3/2}}(\nabla_a + \nabla_c)\phi(a, c) = -\frac{1}{\|a\| (1 - 2\kappa\rho + \rho^2)^{1/2}} \left(-\kappa \frac{a}{\|a\|} + \frac{c}{\|c\|} \right) \quad (47)$$

It follows that, by $\kappa = \frac{a \cdot c}{\|a\| \|c\|}$, (47) is orthogonal to a . This shows that it is sufficient to prove that eq. (46) always has a nonzero component in the direction of a in order to prove that the sum of the two terms never vanishes. We therefore compute

$$((-\nabla_a + \nabla_b)\kappa(a, b))^T a = (\bar{\kappa} + \bar{\rho}) \frac{a^T a}{\|a\|^2} - (\bar{\kappa} + \bar{\rho}^{-1}) \frac{b^T a}{\|b\|^2} = \frac{\|a\|^2 \|b\|^2 - (a^T b)^2}{\|a\| \|b\|^3}.$$

The last term obviously vanishes if and only if $a = \mathbf{y} - \mathbf{x}$ and $b = \mathbf{x} - \mathbf{s}$ are collinear, a case that was discarded in the definition of Ω_2 . Therefore, the component of $(-\nabla_a + \nabla_b)\kappa(a, b)$ in the direction of a is nonzero for $\mathbf{z} \in \Omega_2$. We have proved that the gradient $\nabla_{\mathbf{x}}\psi$ and thus also $\partial_{\mathbf{z}}\Psi$ do not vanish, therefore Ψ is a phase function.

It remains to prove that the phase is non-degenerate. The necessary condition is always satisfied as

$$\partial_{\mathbf{z}, \lambda, \theta}(\partial_\sigma \Psi) = (\partial_{\mathbf{z}}\psi + \partial_\theta\psi - d\lambda) d\sigma \neq 0.$$

As $\Omega_2 \subset \mathbb{R}^4$ open and $\Theta \subset \mathbb{R}$ open, it holds $n = 4$, $m = 2$ and $\mathcal{L}_2^{\tilde{n}_e}$ is an FIO of order

$$\frac{1}{2} - \frac{4+2}{4} = -1.$$

□

Proof of Theorem 12. In view of Theorem 11 and Lemma 7, it remains to show that the vectors

$$\begin{pmatrix} \nabla_{\mathbf{x}}\psi \\ \nabla_{\mathbf{y}}\psi \end{pmatrix}, \begin{pmatrix} \partial_\theta \nabla_{\mathbf{x}}\psi \\ \partial_\theta \nabla_{\mathbf{y}}\psi \end{pmatrix} \quad (48)$$

are linearly independent for every $(\mathbf{d}(\theta), \mathbf{x}, \mathbf{y})$, $\theta \in \Theta$, $(\mathbf{x}, \mathbf{y}) \in \Omega_2$.

We can recycle some of the computations in the proof of Theorem 11. It suffices to show that already the first two components of the gradients are linearly independent to prove the Theorem.

The first two components of the first vector, $\nabla_{\mathbf{x}}\psi$, were computed in eq. (45) and split up into two parts:

$$\nabla_{\mathbf{x}}\psi = r_1(a, b) + r_2(a, c),$$

where $r_1(a, b)$ given in eq. (46), depending only on $a = \mathbf{y} - \mathbf{x}$ and $b = \mathbf{x} - \mathbf{s}$, and $r_2(a, c)$ given in eq. (47), depending only on a and $c = \mathbf{d}(\theta) - \mathbf{x}$. We then argued that $r_2(a, c)^T a = 0$.

Consider now the second vector

$$\partial_\theta \nabla_{\mathbf{x}}\psi = \partial_\theta r_1(a, b) + \partial_\theta r_2(a, c).$$

$r_1(a, b)$ does not depend on θ at all, so $\partial_\theta r_1(a, b) = 0$. The second part $r_2(a, c)$ is always orthogonal to a and so is its derivative $\partial_\theta r_2(a, c)$.

The vector $\partial_\theta \nabla_{\mathbf{x}}\psi$ is thus a multiple of a^\perp , and so is $r_2(a, c)$. In order to prove that $\partial_\theta \nabla_{\mathbf{x}}\psi$ and $\nabla_{\mathbf{x}}\psi$ are linearly independent, it is therefore sufficient to show that $r_1(a, b)$ has a nonzero component in the direction of a . But this leads us back to the proof of Theorem 11, where we studied this exact case and showed that it is always satisfied when $\mathbf{y} - \mathbf{x}$ and $\mathbf{x} - \mathbf{s}$ are not collinear, namely when $(\mathbf{x}, \mathbf{y}) \in \Omega_2$. This proves the Theorem. □

References

- [1] R Acar and C R Vogel. “Analysis of bounded variation penalty methods for ill-posed problems”. In: *Inverse Problems* 10.6 (1994), pp. 1217–1229.
- [2] Martin Burger and Stanley Osher. “A guide to the TV zoo”. In: *Level Set and PDE-based Reconstruction Methods*. Ed. by Osher Stanley Burger Martin. Lecture Notes in Mathematics. 2013, pp. 1–70.
- [3] Javier Cebeiro et al. “On a three dimensional Compton scattering tomography system with fixed source”. In: *arXiv e-prints*, arXiv:2006.14192 (June 2020). arXiv: 2006.14192 [math.NA].
- [4] Clémence Driol. “Imagerie par rayonnement gamma diffusé à haute sensibilité”. PhD thesis. Université de Cergy-Pontoise, 2008.
- [5] B. L. Evans et al. “Nondestructive inspection using Compton scatter tomography”. In: *1997 IEEE Nuclear Science Symposium Conference Record*. Vol. 1. 1997, 386–390 vol.1.
- [6] C. Geiger and C. Kanzow. *Numerische Verfahren zur Lösung unrestringierter Optimierungsaufgaben*. Springer-Lehrbuch. Springer Berlin Heidelberg, 1999.
- [7] B. N. Hahn. “Reconstruction of dynamic objects with affine deformations in computerized tomography”. In: *Journal of Inverse and Ill-posed Problems* 22.3 (2014), pp. 323–339.

- [8] B. N. Hahn and M.-L. Kienle Garrido. “An efficient reconstruction approach for a class of dynamic imaging operators”. In: *Inverse Problems* 35.9 (2019), p. 094005.
- [9] Lars Hörmander. “Fourier integral operators. I”. In: *Acta Math.* 127 (1971), pp. 79–183.
- [10] Nobuyuki Kanematsu, Taku Inaniwa, and Minoru Nakao. “Modeling of body tissues for Monte Carlo simulation of radiotherapy treatments planned with conventional x-ray CT systems”. In: *Physics in Medicine and Biology* 61.13 (2016), pp. 5037–5050.
- [11] Oskar Klein and Yoshio Nishina. “Über die Streuung von Strahlung durch freie Elektronen nach der neuen relativistischen Quantendynamik von Dirac”. In: *Zeitschrift für Physik* 52.11 (1929), pp. 853–868.
- [12] Hermann Kolanoski and Norbert Wermes. *Teilchendetektoren: Grundlagen und Anwendungen*. Springer, 2016.
- [13] Venkateswaran P. Krishnan and Eric Todd Quinto. “Microlocal Analysis in Tomography”. In: *Handbook of Mathematical Methods in Imaging*. Ed. by Otmar Scherzer. New York, NY: Springer New York, 2015, pp. 847–902.
- [14] P Kuchment, K Lancaster, and L Mogilevskaya. “On local tomography”. In: *Inverse Problems* 11.3 (1995), pp. 571–589.
- [15] Claude Leroy and Pier-Giorgio Rancoita. *Principles of radiation interaction in matter and detection*. Singapore: World Scientific, 2011.
- [16] F. Natterer. *The Mathematics of Computerized Tomography*. Society for Industrial and Applied Mathematics, 2001.
- [17] Frank Natterer and Frank Wübbeling. *Mathematical Methods in Image Reconstruction*. Society for Industrial and Applied Mathematics, 2001.
- [18] M K Nguyen and T T Truong. “Inversion of a new circular-arc Radon transform for Compton scattering tomography”. In: *Inverse Problems* 26.6 (2010), p. 065005.
- [19] Stephen J. Norton. “Compton scattering tomography”. In: *Journal of Applied Physics* 76.4 (1994), pp. 2007–2015.
- [20] V P Palamodov. “An analytic reconstruction for the Compton scattering tomography in a plane”. In: *Inverse Problems* 27.12 (2011), p. 125004.
- [21] Gaël Rigaud. “3D Compton scattering imaging: study of the spectrum and contour reconstruction”. In: *arXiv e-prints*, arXiv:1908.03066 (2019). arXiv: 1908.03066 [math.NA].
- [22] Gaël Rigaud. “Compton Scattering Tomography: Feature Reconstruction and Rotation-Free Modality”. In: *SIAM Journal on Imaging Sciences* 10 (2017), pp. 2217–2249.
- [23] Gaël Rigaud and Bernadette N Hahn. “3D Compton scattering imaging and contour reconstruction for a class of Radon transforms”. In: *Inverse Problems* 34.7 (2018), p. 075004.
- [24] Leonid I. Rudin, Stanley Osher, and Emad Fatemi. “Nonlinear Total Variation Based Noise Removal Algorithms”. In: *Phys. D* 60.1–4 (1992), pp. 259–268.
- [25] J. P. Stonestrom, R. E. Alvarez, and A. Macovski. “A Framework for Spectral Artifact Corrections in X-Ray CT”. In: *IEEE Transactions on Biomedical Engineering* BME-28.2 (1981), pp. 128–141.
- [26] Cecilia Tarpau et al. “Analytic inversion of a Radon transform on double circular arcs with applications in Compton Scattering Tomography”. In: *IEEE Transactions on Computational Imaging* PP (2020), pp. 1–1.
- [27] N. Uhlmann et al. “Metrology, Applications and Methods with High Energy CT Systems”. In: (2014).
- [28] James Webber. “X-ray Compton scattering tomography”. In: *Inverse Problems in Science and Engineering* 24 (2015), pp. 1323–1346.
- [29] James Webber and Eric Todd Quinto. “Microlocal analysis of a Compton tomography problem”. In: *arXiv e-prints*, arXiv:1902.09623 (2019). arXiv: 1902.09623 [math.FA].